

Light-Harvesting in Biophotonic Optofluidic Microcavities via Whispering-Gallery Modes

Zhiyi Yuan, Xin Cheng, Tsungyu Li, Yunke Zhou, Yifan Zhang, Xuerui Gong, Guo-En Chang, Muhammad D. Birowosuto, Cuong Dang, and Yu-Cheng Chen*



Cite This: <https://doi.org/10.1021/acsami.1c09845>



Read Online

ACCESS |



Metrics & More

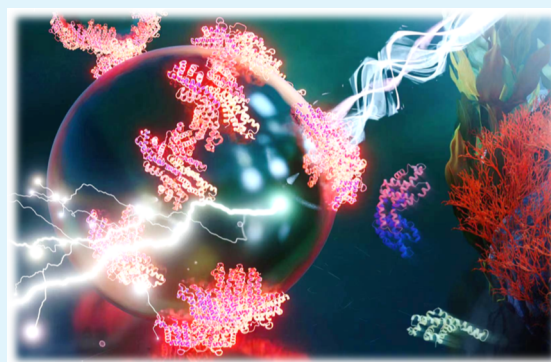


Article Recommendations



Supporting Information

ABSTRACT: Phycobiliproteins are a class of light-harvesting fluorescent proteins existing in cyanobacteria and microalgae, which harvest light and convert it into electricity. Owing to recent demands on environmental-friendly and renewable apparatuses, phycobiliproteins have attracted substantial interest in bioenergy and sustainable devices. However, converting energy from biological materials remains challenging to date. Herein, we report a novel scheme to enhance biological light-harvesting through light–matter interactions at the biointerface of whispering-gallery modes (WGMs), where phycobiliproteins were employed as the active gain material. By exploiting microdroplets as a carrier for light-harvesting biomaterials, strong local electric field enhancement and photon confinement at the cavity interface resulted in significantly enhanced biophotocurrent. A threshold-like behavior was discovered in photocurrent enhancement and the WGM modulated fluorescence. Systematic studies of biologically produced photoelectricity and optical mode resonance were carried out to illustrate the impact of the cavity quality factor, structural geometry, and refractive indices. Finally, a biomimetic system was investigated by exploiting cascade energy transfer in phycobiliprotein assembly composed of three light-harvesting proteins. The key findings not only highlight the critical role of optical cavity in light-harvesting but also offer deep insights into light energy coupling in biomaterials.



KEYWORDS: light-harvesting, whispering-gallery mode, optofluidic microcavity, energy coupling, biological fluorescent proteins

INTRODUCTION

Fluorescent proteins have emerged as an active material with a promising functionality in biological applications and photonic devices over the past decade.^{1–5} One of the most well-known fluorescent proteins is the green fluorescent protein, which has been extracted from jellyfish (*Aequorea victoria*) and is now commonly used for engineering cells and molecules.⁶ Another family of fluorescent proteins which are capable of harvesting light and converting it into electricity through biochemical machinery is called phycobiliproteins. Such proteins are widely involved in photosynthetic light-harvesting antenna complex of cyanobacteria and microalgae.⁷ Owing to its unique light-emitting and photosynthetic properties, phycobiliproteins have demonstrated promising potential in biotechnology and solid-state devices.^{8–10} Recent demands for environmental-friendly materials and energy renewability have further driven the field in bioenergy devices. In this frame, photoactive structures and light-harvesting proteins, such as phycobiliproteins, can be envisaged as the most perfected materials. One of the key efforts is optimization of the light-harvesting and conversion efficiencies.

The development of a light-harvesting apparatus has been at the heart of organic photonic and optoelectronic devices. In

order to enhance the photon conversion efficiency, various schemes have been elaborated, involving the use of plasmonic nanoparticles,^{11–13} metasurfaces,¹⁴ and resonant cavities.^{15–18} To date, whispering-gallery mode (WGM) microcavities have garnered broad interest due to the significantly prolonged photon lifetime as a result of total internal reflection between the resonant cavity and the surrounding medium. Thanks to the extremely high quality factor (*Q*-factor) and enhanced light–matter interaction, WGM microcavities have been extensively explored in biosensing,^{19–23} imaging,^{24,25} solar cells,^{26–28} and photocatalytic applications.²⁹ In comparison to the vast majority of passive resonators, active resonators containing a gain medium have emerged as a promising tool to amplify biological signals through optical emissions, such as optofluidic biolasers.^{23,30–36} Although several milestones in WGM microcavities have been achieved, the possibility of

Received: May 27, 2021

Accepted: July 12, 2021

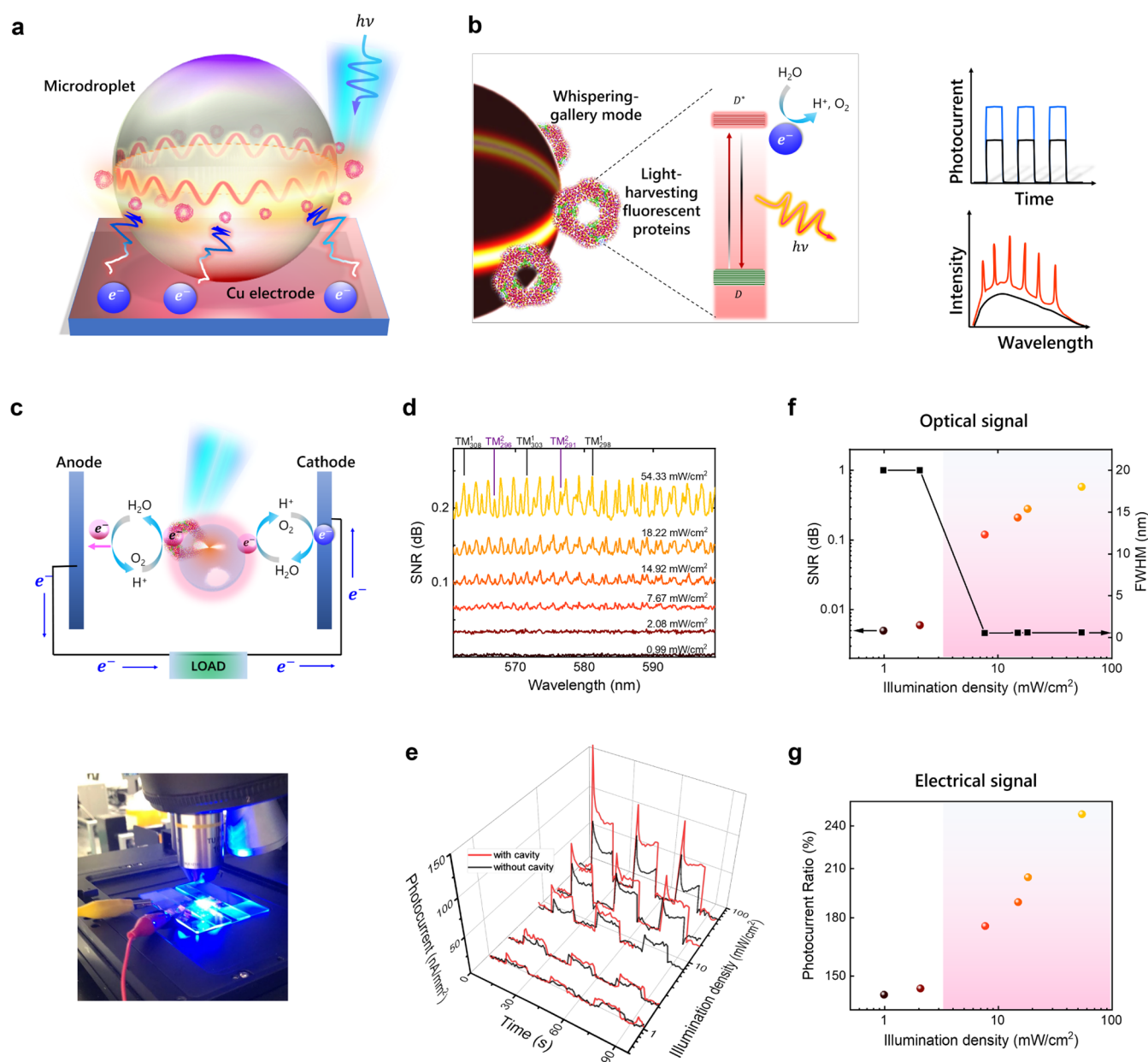


Figure 1. (a) Schematic illustration of the WGM-enhanced photoelectricity from light-harvesting protein microcavity assemblies. The phycobiliproteins are adhered to the external surface of LC microdroplets and excited by LED light. (b) Fundamental mechanism of WGM-enhanced photoelectricity, in which the phycobiliproteins absorb photons and then produce photons and electrons. Enhanced bio-photoelectricity and modulated fluorescence emission are expected owing to the WGM. (c) Top: schematic diagram showing the working principle and the structure of the device which comprises two separated copper tape electrodes to harvest the electrons. The anode and the cathode are connected to a potentiostat via spring-loaded clips in a two-electrode measurement setup. Bottom: photograph of the device being excited by blue light. (d) Fluorescence background-subtracted spectra of RPE based on a single microdroplet illuminated by blue light under different illumination densities. The spectra were accumulated 10 times, and the curves are vertically shifted for clarity. (e) Photocurrent measured vs time from RPE illuminated by blue light under different illumination densities, without the WGM cavity and with WGM cavities. The red line and the black line represent the photocurrent with and without the WGM cavity, respectively. (f) SNR extracted from (d) as a function of illumination density. (g) Photocurrent ratio as a function of the illumination density derived from (e).

exploiting WGM cavities to amplify biological electricity has never been explored.

In this study, we report a novel scheme to enhance biological light-harvesting through light–matter interactions at the biointerface of optical microcavities. The concept of light-harvesting protein microcavity assemblies by exploiting WGMs is illustrated in Figure 1a. Due to the energy coupling between the WGM cavity and photosynthetic fluorescence, the photocurrent increased significantly as the pump increases,

which is similar to that of modulated fluorescence. Our results demonstrate that the biological photocurrent increases as the microcavity Q -factor increases, which can be attributed to the strong photon confinement and electric field enhancement at the cavity surface. By utilizing the tunable optical and structural properties of liquid crystal (LC) droplets, we systematically investigated the impact of the optical microcavity on photocurrent generation, including the internal cavity structures, refractive indices, and resonator sizes. Both the

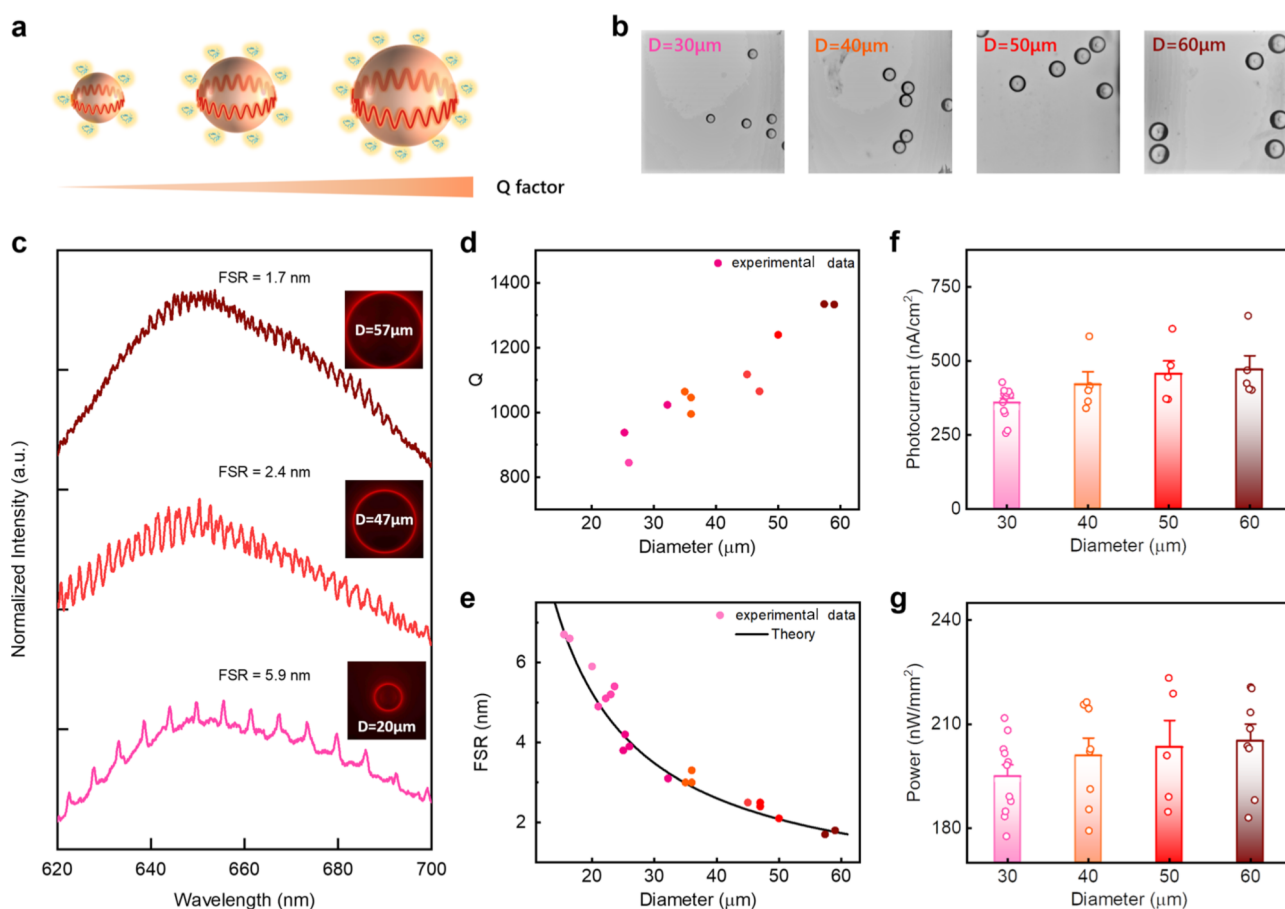


Figure 2. (a) Schematic diagram showing WGM microcavities of different sizes, in which CPC molecules are attached to the droplet surface. (b) CCD images of LC microdroplets in the part of the device corresponding to different LC WGM cavity sizes. The microdroplets maintain the same size in a single measurement. (c) Modulated fluorescence spectra of CPC based on a single microdroplet with different cavity diameters. The insets show the corresponding fluorescence images of microdroplets. The spectra were accumulated 15 times. (d) Q -factor as a function of the microdroplet diameter. (e) FSR as a function of the microdroplet diameter. The solid line was calculated using the formula: $FSR = \lambda^2/n_{\text{eff}}\pi D$. (f) Comparison between the photocurrent obtained from CPC with various microdroplet sizes. (g) Comparison between the power obtained from CPC with different microdroplet sizes.

experimental and simulation results verified that electric field enhancement formed by the resonant microcavity largely contributes to photocurrent generation. Finally, to demonstrate the potential application of light-harvesting protein microcavity assemblies, a biomimetic system was explored by using a phycobiliprotein complex composed of three major light-harvesting proteins [R-phycoerythrin (RPE), C-phycoyanin (CPC), and allophycocyanin (APC)]. With the existence of the Förster resonant energy transfer (FRET) effect, the light energy was captured and funneled efficiently into the resonant cavity surface to generate abundant photoelectricity. The discovery made in this study exhibits the critical role of the WGM microcavity in amplifying the photoelectric energy in light-harvesting biomaterials. The concept can be widely applied to potential areas such as bioinspired devices, artificial photosynthesis, and bioenergy applications.

RESULTS AND DISCUSSION

Concept of Light-Harvesting Protein Microcavity Assemblies. To begin with, we explored the possibility of obtaining amplified photoelectricity with WGM optical microcavities. Figure 1a,b illustrates the concept of using a WGM microcavity to boost the photoelectricity generated

from light-harvesting photosynthetic proteins adhered to the surface. As shown in Figure 1b, both fluorescence emissions and photocurrents are generated simultaneously when the fluorescent proteins are excited by light. Owing to the strong local electric field enhancement and photon confinement at the cavity interface, the emitted photons will be enhanced by the WGM cavity and collected by the spectrometer, while the generated electrons will be collected by the electrodes beneath the droplet. Both optical signals and electrical signals were analyzed. A detailed working mechanism is illustrated in Figure 1c. A microscope with blue light-emitting diode (LED) light was used to illuminate the photosynthetic apparatus placed on the split-copper electrode device. Electron donors are contributed by the H_2O molecule in the phosphate-buffered saline (PBS) solution, while electron acceptors are contributed by O_2 in water. Upon light excitation, electrons produced by light-harvesting proteins will be transported to the anode and generate an electric current flowing to the cathode. Note that the electrons produced by light-harvesting proteins should transfer to the electrode surface through the PBS buffer since the electron transport capability in PBS solution is several orders larger than that in LCs (LC: 10^{-10} to 10^{-12} S/cm; PBS: 10^{-2} S/cm).³⁷ To demonstrate the coupling between the WGM cavity and photosynthetic fluorescent proteins, RPE was

selected as a proof-of-concept to serve as the active material. Figure 1d presents the background-subtracted WGM-modulated fluorescence spectra when the fluorescent RPE molecules adhere to the droplet, resulting in strong evanescent fields between the resonant cavity and RPE. In the presence of the WGM cavity (LC microdroplets), the measured photocurrents of the RPE solution were found to be significantly larger than those measured without the WGM cavity, as shown in Figure 1e. Note that the WGM-modulated fluorescence spectra were collected from a single microdroplet due to the experimental setup.

In order to demonstrate the correlation between the modulated fluorescence and photocurrent, we further studied the WGM spectra and photocurrent under various illumination densities in Figure 1f,g, respectively. In Figure 1d, the intensity of WGM cavities becomes stronger as the illumination density increases, resulting in a higher signal-to-noise ratio (SNR). This result is consistent with the previous research.^{38,39} Meanwhile, the full width at half-maximum (fwhm) of fluorescence decreased rapidly when the illumination density reaches above 2.08 mW/cm². (Detailed calculation for fwhm is provided in Figure S1.) The rapid reduction of fwhm represents the transition from fluorescence to the modulated fluorescence. The sum of SNR and of fwhm extracted from Figure 1d are plotted in Figure 1f, indicating a threshold-like behavior for the WGM-modulated fluorescence. The threshold-like behavior of the SNR and the fwhm is mainly due to the losses compensated by the gain input (higher pump energy). At lower illumination densities, the losses are relatively large due to the optical scattering and material absorption. Thus, one can barely observe the WGM-modulated fluorescence peaks at low pump energies (Figure S1a). At higher illumination densities, an increased amount of fluorescence generated from the light-harvesting proteins couples with the WGM resonance, so that the losses are compensated. On the other hand, the photocurrents measured with and without the WGM cavity are compared in Figure 1e, where the photocurrent enhancement significantly increased beyond an illumination density of 2.0 mW/cm². The sum of photocurrent enhancement (ratio) extracted from Figure 1e is plotted in Figure 1g, revealing a threshold-like behavior similar to that of the WGM-modulated fluorescence. At lower illumination densities, the photocurrent enhancement produced by the WGM cavity remains similar; however, the photocurrent enhancement increased dramatically at higher illumination densities owing to WGM resonance. We would like to emphasize that when we compared the photoelectricity without cavity and with cavity in the article, the total number of protein molecules in the active region of illumination is the same for the entire article. To exclude effective absorbance enhancement due to protein aggregation on the surface of droplets, we have measured the fluorescence generated from a single droplet and compared it with its surrounding bulk medium (Figure S2). As one can see, the modulated fluorescence peaks demonstrate that the total proteins attached to the surface only generate a total emission intensity similar to that of the surrounding medium. We note that the protein may aggregate on the droplet surface, but there are almost no protein molecules inside the droplet. However, the photoelectricity still shows a much larger enhancement as compared to the surrounding medium. Additionally, we studied the correlation between the fluorescence and the photocurrent at different excitation wavelengths (Figure S3). The fluorescence

intensity under different excitation wavelength bands correlated well with the photocurrent density. The optimal absorption of light will lead to a larger photocurrent. The stability of the photocurrent produced by light-harvesting protein microcavity assemblies is also considered (Figure S4). The results clearly show that the photocurrent output maintains stability before aqueous evaporation.

Investigation of the Effect of Q-Factor on Photoelectricity Generation. Next, we systematically studied the relationship between the optical cavity resonance and the light-harvesting-protein-generated photoelectricity. In Figure 2, we investigated the impact of the cavity *Q*-factor by adjusting the WGM droplet cavity size. The schematic in Figure 2a shows that the optical *Q*-factor changes with the diameter of droplets. LC droplets with four different sizes were prepared with a microfluidic chip (controlled size of droplets), as shown in Figure 2b. Thanks to the evanescent field existing at the interface between the microcavity and proteins, the WGM-modulated fluorescence spectra from the fluorescent protein CPC were compared for different droplet sizes (Figure 2c). Based on different cavity diameters, the corresponding *Q*-factor was calculated and measured (Figure S5). Note that the *Q*-factor we measured (free-space coupling) is the far-field component which is not equal to the intrinsic *Q*-factor of the cavity. The far-field component of the *Q*-factor is determined by the surface scattering, and we can collect the modulated spectra only when the scattering rate is faster than or comparable to the internal loss mechanisms (low far-field *Q*-factor). Owing to the fact that the reciprocal of the total *Q*-factor of WGM cavity is the reciprocal sum of all components of *Q*, the total *Q*-factor is determined from the relatively low components of the *Q*-factor. Therefore, the far-field component of the *Q*-factor can affect the total *Q*-factor in our spectral measurement regime.⁴⁰ Figure 2d demonstrates the average *Q*-factor as a function of microdroplet diameter, in which the *Q*-factor increases as the diameter increases. It is well known that the *Q*-factor of the optical cavity represents its capability in photon confinement and electric field enhancement. As such, the trend in Figure 2d reveals that larger microdroplets possess higher photon confinement capability and electric field enhancement. The free spectral range (FSR) value decreases with the increment of the droplet diameter, as plotted in Figure 2e. This agrees well with the theoretical calculation of $FSR = \lambda^2/n_{\text{eff}}\pi D$,^{41,42} where λ is the wavelength, n_{eff} is the effective refractive index, and D is the WGM cavity diameter. The corresponding photocurrent and power obtained for various cavity sizes (*Q*-factors) are presented in Figure 2f,g. Although the number of proteins on the surface of a single droplet increases while the droplet diameter increases, the density of the LC volume in water was controlled for various diameter groups. As such, the total surface volume which could be generated will increase with the number of droplets (after forming into droplets). Note that the surface-to-volume ratio increases as the droplet diameter decreases. The smaller droplets have a larger surface-to-volume ratio and thus will have a larger effective surface area (and molecules) involved in the WGM. Under the same conditions, the photocurrent and power increased unambiguously, reflecting a higher capability to generate photoelectricity with a higher *Q*-factor.

In addition to optical cavity *Q*-factors, we studied how the number of optical resonators will influence the output of electricity. The photocurrent produced by CPC with different

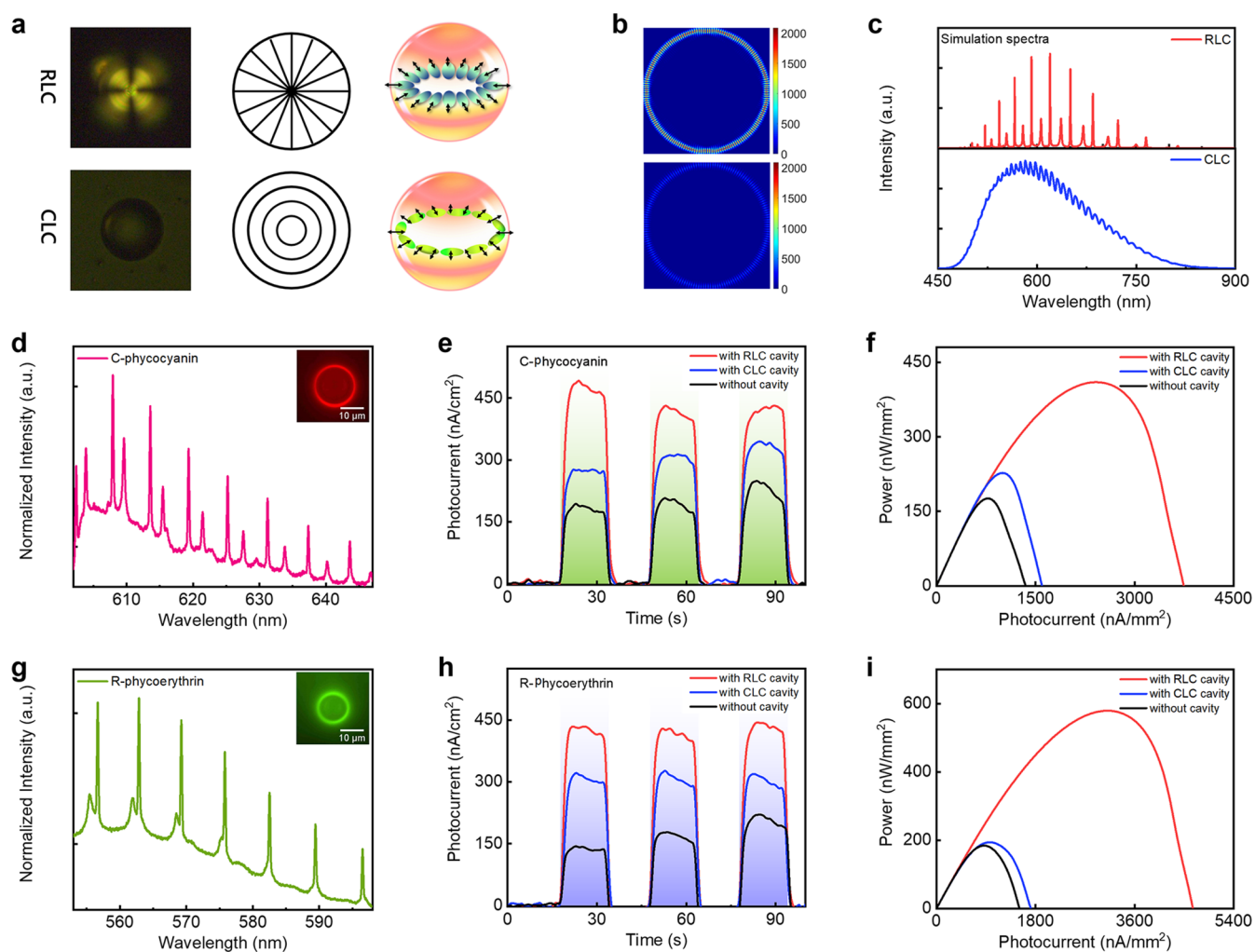


Figure 3. (a) Comparison between RLC and CLC microdroplets. Left: CCD images of RLC (top) and CLC (bottom). Middle: configuration diagrams of RLC (top), in which LC molecules are parallel to the radial orientation, and CLC (bottom), in which LC molecules are perpendicular to the radial orientation. Right: schematic diagrams of the electric field direction of TM modes in RLC (top) and CLC (bottom). The green prolate ellipsoid represents the uniaxial dielectric tensor of the LC. (b) FDTD numerical simulations of $10\ \mu\text{m}$ diameter WGM resonators displaying the electric field distribution (internal refractive indexes are equal to 1.71 and 1.54). (c) Simulated fluorescence spectra of RLC and CLC. (d) Experimental modulated fluorescence spectra of CPC based on a single microdroplet. The inset shows the fluorescence image. The spectra were accumulated 30 times. (e) Photocurrent measured vs time from CPC illuminated by green light, without a cavity and with CLC and RLC cavities. (f) Power vs photocurrent of CPC without a cavity and with CLC and RLC cavities (applied voltage, 0–300 mV). (g) Modulated fluorescence spectra of RPE based on a single microdroplet. The inset shows the fluorescence image illuminated by blue light. The spectra were accumulated 30 times. (h) Photocurrent vs time of RPE, without a cavity and with CLC and RLC cavities. (i) Power vs photocurrent when RPE was deposited onto the device without a cavity and with CLC and RLC cavities (applied voltage, 0–300 mV).

numbers of WGM resonators (Figure S6a), where all the microdroplets are fixed under the same diameter (see Methods and Materials). Under specified conditions, photocurrents of 385, 414, and 474 nA/cm^2 were obtained, respectively, as the number of microdroplets increases. This trend can be attributed to the increasing amount of WGM microcavities since more light-harvesting proteins are coupled to WGM resonance and thus more photocurrent can be obtained. However, the LC itself does not play a role here for electron transport due to low electron transportability (10^{-10} to 10^{-12} S/cm) compared to that of PBS solution. To confirm this effect, the photocurrent with different volumes of pure LC solutions was measured (Figure S6b). A decreasing trend of photocurrent was observed when additional LC was added to the solution. Note that the interfacial electron transport rate is only dependent on the interface between the electrolyte and the electrode in this study. Since all the electrodes and

electrolytes were fixed in all experiments, the interfacial electron transport rate should not alter for different measurements.

Investigation of the Effect of Refractive Index on Photoelectricity Generation. Subsequently, we investigated how the geometry and the refractive index of the optical cavity may have an impact on the photocurrent, I – V curves, and power performance. Taking advantage of the tunable structural properties of LC droplets, we prepared two types of LC microcavities with nematic and cholesteric LC materials. Figure 3a shows the schematic diagrams and polarized optical images of the two cavities, the radial-oriented LC (RLC) droplet and the cholesteric LC (CLC) droplet. Note that the transverse magnetic (TM) modes and transverse electric modes in WGM polarizations correspond to the electric field oscillating in parallel and perpendicular to the radial orientation, respectively (Figure S7). To evaluate the optical

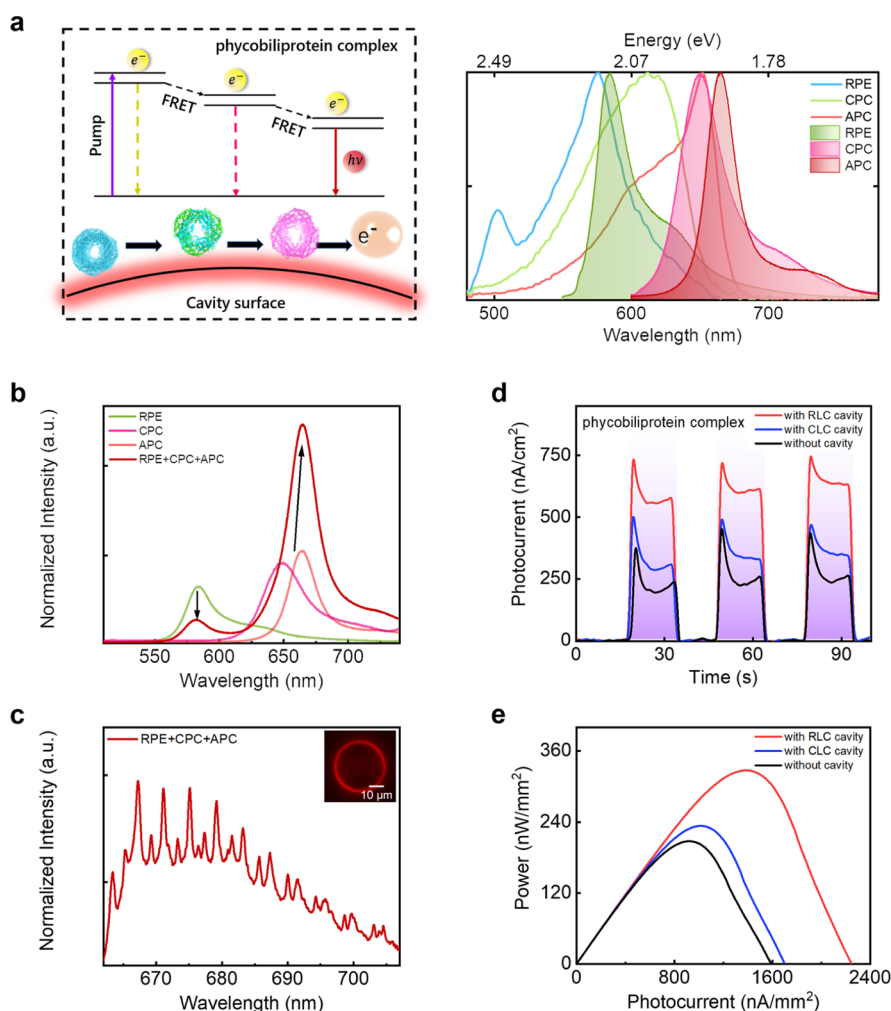


Figure 4. (a) Left: schematic diagram illustrating the energy transfer in the phycobiliprotein complex composed of RPE, CPC, and APC. Right: normalized absorption spectra and emission spectra of the three phycobiliproteins. (b) Fluorescence emission spectra of RPE, CPC, APC, and the phycobiliprotein complex. All the concentrations were fixed at 0.13 mg/ml. (c) Modulated fluorescence spectra of the phycobiliprotein complex based on a single microdroplet. The inset shows the corresponding fluorescence image of a single microdroplet when excited by UV light. (d) Photocurrent vs time measured for the phycobiliprotein complex, without a cavity and with CLC and RLC cavities. (e) Power vs photocurrent for the phycobiliprotein complex without a cavity and with CLC and RLC cavities (applied voltage, 0–300 mV).

resonance difference among the RLC and CLC droplets, the finite difference time domain (FDTD) method was utilized to simulate the WGM electric field distribution and the WGM spectrum, as shown in Figure 3b,c (see Methods and Materials). In theory, the RLC droplet possesses a much stronger resonance than the CLC droplet due to a higher refractive index in terms of TM modes. Experimentally, a stronger modulated fluorescence was also observed from RLC upon binding to fluorescent proteins (Figure S8), as compared to CLC. Note that the difference between the SNR peaks of RLC and CLC is much smaller than the simulation one in Figure 3c due to many experimental factors. Herein, the abovementioned two LC cavities represent strong optical resonance and weak optical resonance, respectively. To compare the resonance effect, we used two different fluorescent proteins as the light-harvesting gain material in the following analysis.

Figure 3d displays the WGM-modulated fluorescence spectra from CPC based on the RLC microcavity. The photocurrents generated from CPC under green light excitation are shown in Figure 3e, by comparing in the

presence of different cavities and without cavity over three cycles. In this part, the microdroplets in one group were not of the exact same size since we used the vortex method to prepare the LC microdroplets. With a fixed control of other variables, a photocurrent of 186 nA/cm² was observed without the WGM cavity. To our surprise, photocurrents of 278 and 496 nA/cm² were obtained with the introduction of CLC and RLC microcavities, respectively. It is noteworthy that a significant improvement of more than 250% was achieved in photocurrent when the fluorescence was modulated by the RLC cavity, while only 150% enhancement was obtained with the CLC cavity. Furthermore, similar improvements were observed in the polarization curves (Figure S9a). A peak power of 410 nW/mm² was obtained from the RLC cavity, which is improved by 230% (Figure 3f). The same experiment was conducted again by changing the fluorescent protein to RPE. Figure 3g shows the WGM-modulated fluorescence spectra from RPE based on the RLC microcavity. The photocurrents resulting from RPE under blue light excitation are shown in Figure 3h, wherein photocurrents of 175, 316, and 429 nA/cm² were observed for without a cavity, with the CLC cavity, and with the RLC cavity,

respectively. Similar to the results shown in Figure 3e, the photocurrent increased remarkably around 250% in the presence of a cavity compared to that obtained without a cavity. The same trend can be observed in the polarization curves (Figure S9b). A peak power of 580 nW/mm² was reached when RPE emission was modulated by the WGM microcavity, demonstrating a significant enhancement by over 300% (Figure 3i).

Applications of Light-Harvesting Protein Microcavity Assemblies. Finally, we employed this mechanism in a biomimetic system to demonstrate the potential application of light-harvesting protein microcavity assemblies. Phycobiliproteins are the fluorescent components of the photosynthetic light-harvesting antenna complexes of cyanobacteria, algae, and cryptomonads. Three major categories of phycobiliproteins, including RPE, CPC, and APC, can be classified according to their absorption energy. Taking advantage of the FRET effect, the light energy can be harvested more efficiently to the microcavity surface. Herein, we investigated the bio-photo-electrical transfer based on this biomimetic structure.

Figure 4a shows the schematic diagram of the three light-harvesting proteins, including RPE, CPC, and APC. The normalized absorption and emission spectra corresponding to three light-harvesting proteins are also shown in the right panel of Figure 4a. When three proteins were mixed, the fluorescence intensity of RPE was remarkably reduced, while the fluorescence emission from APC was enhanced (Figure 4b). By comparing the fluorescence intensity of donor emission with and without the acceptor, the energy-transfer efficiency can be obtained as 55% ($1 - F_d/F_{da}$). In order to prove that the nonradiative energy transfer occurs between RPE and the other two proteins, we measured the time-resolved fluorescence emission (Figure S10). The lifetime of a donor (RPE) without an acceptor was measured to be $\tau_d = 1.73$ ns, while the donor emission lifetime of the three proteins (donor concentration remains the same) was measured to be $\tau_{da} = 1.29$ ns. According to the FRET efficiency formula ($E_f = 1 - \tau_d/\tau_{da}$), the FRET efficiency can be obtained as 25.4%. It can be noted that when molecules (donor and acceptor) are coupled with the photonic modes, radiative energy transfer plays an important role in the energy-transfer process, resulting in transfer improvement or suppression.^{35,43–45} Therefore, the FRET efficiency and radiative energy-transfer efficiency may be changed on the surface of microdroplet due to the WGM resonance.^{46–48} Next, we immersed the phycobiliproteins with RLC microdroplets to investigate the optical/electrical properties with the WGM cavity. Figure 4c illustrates the WGM-modulated fluorescence spectra, showing that phycobiliproteins adhered to the microdroplet. With the existence of the WGM microcavity, an extremely large photocurrent of 693 nA/cm² was achieved upon ultraviolet (UV) illumination, while only 242 nA/cm² was obtained without the cavity (Figure 4d). This result provided us with improvements of close to 250%, which support the concept of WGM-cavity-enhanced bioenergy harvesting and the potential application on artificial photosynthetic systems. It is noteworthy that without the addition of electron mediators, the effect of the cavity-enhanced photocurrent was still evident. Furthermore, similar improvements were also observed in the polarization curves (Figure S11) and output power curves (Figure 4e), where the increasing downward gradient indicated mass-transfer limitations.

In addition to light-harvesting proteins, the most important key component in photosynthetic light-harvesting is chlorophyll molecules, including chlorophyll *a* and chlorophyll *b* in the reaction center of plants and algae. Finally, we explored the possibility of using WGM microcavities to enhance photoelectric generation by using chlorophyll as the active gain material. As a proof-of-concept, we integrated the photocurrent performance of chlorophylls incorporated with microdroplets (Figure S12). As shown in the results, a significant photocurrent enhancement was obtained, indicating the potential to amplify bio-photocurrents from a wide range of species with chlorophylls.

CONCLUSIONS

In this study, we proposed the concept of WGM-enhanced photoelectricity by exploiting the optical coupling between cavity modes and photosynthetic protein fluorescence. The results demonstrate that biologically produced photoelectricity could be amplified through light-harvesting protein microcavity assemblies, in which phycobiliproteins were employed as the gain medium. For the first time, our findings revealed a threshold-like behavior in modulated fluorescence and photocurrent enhancement, attesting the function of the WGM microcavity in biological light-energy harvesting. Strong local electric-field enhancement and photon confinement at the cavity interface leads to significantly enhanced bio-photoelectricity. Both experimental and simulation results verified that the electric-field enhancement formed by the resonant microcavity would increase photocurrent generation. Finally, a biomimetic system was investigated based on the microcavity to demonstrate the potential application of light-harvesting protein microcavity assemblies by exploiting the phycobiliprotein complex. Our results not only pave the way for future applications in biological electricity generation but also provide comprehensive insights into the relationship between light-harvesting and optical microcavity.

Herein, we would like to discuss several future perspectives for the light-harvesting protein microcavity assemblies. First, the overlap factor for the optical mode and the gain medium are much lower than the value of the gain within the cavity. By doping the light-harvesting biomaterial inside the microdroplet, the overlap factor can be improved. As such, the light-harvesting efficiency can be fully enhanced. Second, WGM resonators can be applied to other systems, such as electrons.^{49,50} By carefully designing the structure of the WGM resonator, conversion efficiency improvement can be achieved through the electron-resonant cavity in the future. Moreover, by further decreasing the mode volume and increasing the *Q*-factor, the energy-transfer rate between excitons and the cavity could be involved in the strong coupling regime.^{18,51,52} We envision that the concept of light-harvesting microcavity may have the potential for studying fundamental physics in photosynthetic energy conversion. Finally, the concept of this work can be further applied to artificial photosynthesis and any other types of photosynthetic apparatuses for electricity generation.⁵³ The facile approach of using a microdroplet as a carrier can simply allow the integration of various photosynthetic apparatuses within the microdroplets to enhance the light-harvesting and conversion efficiencies.

METHODS AND MATERIALS

Light-Harvesting Material Preparation. The photosynthetic proteins used in the work were purchased from Sigma-Aldrich. Stock

solutions of RPE (RPE #52412), CPC (CPC #52468), and APC (APC #A7472) were all diluted with PBS to a final concentration of 0.4 mg/mL. All the proteins were used directly from stock solutions provided by Sigma-Aldrich. Chlorophyll-*a* (Sigma-Aldrich #C5753) was first dissolved in ethanol with a concentration of 1 mg/mL and then diluted with PBS solution to a concentration of 0.1 mg/mL. For preparing the LC microdroplet aqueous solution, 28.8 mg (0.1 mmol) of sodium dodecyl sulfate (SDS) was added to 50 mL of PBS solution. The mixture was stirred magnetically for about 20 min at 1000 rpm to obtain a homogeneous SDS/PBS solution. To prepare the RLC microdroplet emulsion, 20 μ L of LC (nematic liquid crystal, 5CB, 4'-pentyl-4-biphenylcarbonitrile, Sigma-Aldrich #328510) was added to 1 mL of homogeneous SDS/PBS solution. The resulting mixture was mixed by vortexing for 1 min to produce the RLC microdroplet emulsion. For preparing CLC microdroplets, 20 μ L of LC and 10 μ L of chiral dopant [4-cyano-4'-(2-methylbutyl)biphenyl, CB15, Tokyo Chemical Industry #C2913] were mixed first and then added to 1 mL of homogeneous SDS/PBS solution. The resulting mixture was mixed by vortexing for 1 min to produce the CLC microdroplet emulsion. For the preparation of same-sized LC microdroplets in Figure 2, we used a microfluidic chip purchased from uFluidic; it was connected to digital syringe pumps (Fusion 200, Chemyx) (Legato 180, KD Scientific) to enforce a constant flow rate. The two flows meet before entering a narrow channel that opens into the run-off channel. In an appropriate range of flow rates, the center fluid will pinch off to form droplets in the run-off channel. The 5CB LC was used as the dispersed phase, and the SDS/PBS solution was used as the continuous phase. The typical flow rates for the dispersed and continuous phases were set around 2 and 20 μ L/min, which provide LC droplets with a diameter of around 50 μ m. When the flow rate of the dispersed phase is 1.5, 1.8, and 2.2 μ L/min, the droplet diameter is around 20, 30, and 60 μ m, respectively. To produce LC droplets stably, the flow rates of the dispersed phase and the continuous phase should be finely adjusted according to the situation. The fluorescent proteins were then mixed with the prepared LC droplets directly. Fluorescent proteins will therefore adhere to the surface of the LC droplet through physical absorption; this was also confirmed by fluorescence microscopic images in the insets of Figures 2 and 3. In each measurement, the density of LC in the solution was kept constant (2% v/v LC in PBS/SDS solution). In order to control the density of LC droplets in the solution, we shook the microtube before we drop-cast the solution into the device. In Figure S6, we first prepared the LC droplets with microfluidic pumps to fabricate monodisperse-sized droplets in 2% v/v LC in a PBS/SDS solution. Then, we diluted the LC droplets with different concentrations of solutions to obtain different numbers of WGM resonators. The final densities of LC droplets in the solution are 0.5, 1, and 2% v/v, respectively.

Photoelectrochemical Device and Measurements. Copper tapes bought from local hardware stores were used as the electrode material. To create an anode and a cathode, two thin copper tapes were prepared on a transparent glass slide. The resistance of our 6 mm wide copper tape is 0.01 Ω per centimeter. To retain the liquid droplet at the same position and its shape on the device each time, we used two transparent glass slides and UV glue to restrict the fluid flow in the horizontal plane. The potentiostat was then connected via clips and wired in a two-electrode setup, and a microscope with a LED was used to illuminate the photosynthetic apparatus.

The photocurrents produced by the photosynthetic protein and chlorophyll-*a* were measured within the setup. Toothless crocodile clips with a prototyping wire were then used to connect to the potentiostat leads. 10 μ L of LC droplets in the SDS/PBS solution mixture with 10 μ L of the photosynthetic protein solution or chlorophyll-*a* solution was deposited onto the Cu electrodes. For measuring the photocurrent in the deformed LC solution, 10 μ L of the SDS/PBS solution mixture with 10 μ L of the photosynthetic protein solution or chlorophyll-*a* solution was deposited onto the Cu electrodes and then 0.5 μ L of LC was added to keep almost the same LC/water ratio, as compared to the previous experiments.

Upon preparation of the device, the device was integrated with an LED microscope system. The light was fixed with a beam area of 0.07 cm². To generate appropriate photocurrents, UV light (365–420 nm) was used for chlorophyll-*a*; blue light (465–495 nm); green light (540–580 nm); and red light (600–640 nm) were used for RPE and CPC, respectively. To generate a potential between the electrodes, we focused the LED light on one copper tape each time. The light was turned on for approximately 15 s, then off for 15 s and this was repeated for a total of three cycles to illustrate the photoresponsive nature of the device fully. All the photocurrent experiments were collected by a Zahner Zennium potentiostat in the chronoamperometry mode, set to 0 V to maximize current without biasing it. *I*–*V* and power curves were collected with the same potentiostat setup in the linear sweep voltammetry mode at a scan rate of 10 mV/s with no dwell time. The power was determined by multiplying the voltage and the current (Ohm's law). All experiments were run in open air at room temperature.

Optical System Setup. To illuminate the photosynthetic apparatus, the device was placed atop a microscope slide and mounted on a Nikon NI-E microscope with a 10 \times 0.3 NA objective set. Excitation light was generated by an attached LED and filtered for cubes with different filters, as appropriate. Both bright-field and fluorescence images were collected with a Touptek CCD camera, while the fluorescence spectra were collected using an Andor Kymera 328i/Newton 970 EMCCD spectrophotometer. For the WGM-modulated fluorescence spectra measurement, a 100 \times 1.3 NA objective was used for both the excitation and the collection of the fluorescence. In order to reduce the noise, we accumulated the 0.5 s time-integrated spectra by 10–30 times. The absorbance spectra were collected using an Implen N60 nanophotometer.

Simulation Information. The electric field intensity distribution and the spectrum in a single microspher were calculated by FDTD simulation (FDTD Solutions, Lumerical Solutions, Inc). The structure consists of a microsphere (10 μ m diameter) with dipoles (electric dipole or magnetic dipole; emission: 500–800 nm) located at the surface of the microsphere. The WGM cavities were excited by the dipoles on the surface of the microsphere.⁵⁴ To detect the electric field distribution, we used a frequency-domain field profile monitor. To detect the spectrum, we used a field time monitor. It can be noted that the electric field intensity showed different values at different wavelengths or different numbers of dipoles. Thus, the number of dipoles and the resonance wavelength should remain the same in order to compare with the RLC and the CLC.

■ ASSOCIATED CONTENT

Supporting Information

The Supporting Information is available free of charge at <https://pubs.acs.org/doi/10.1021/acsami.1c09845>.

Original fluorescence spectra; modulated fluorescence spectra of a single microdroplet and the bulk solution; correlation between RPE fluorescence and short-circuit current; stability of light-harvesting protein microcavity assemblies; calculation method of average *Q*-factor; photocurrent at different microcavity numbers or LC volumes; LC molecular orientation and WGM polarization schematics; experimental fluorescence spectra of RLC and CLC; applied potential versus photocurrent of CPC and RPE; time-resolved fluorescence emission measurement; applied potential versus photocurrent of the light-harvesting protein complex; WGM-modulated fluorescence spectra; and photocurrent of chlorophyll-*a* (PDF)

AUTHOR INFORMATION

Corresponding Author

Yu-Cheng Chen – School of Electrical and Electronics Engineering, Nanyang Technological University, 639798, Singapore; School of Chemical and Biomedical Engineering, Nanyang Technological University, 637459, Singapore; orcid.org/0000-0002-0008-5601; Email: yucchen@ntu.edu.sg

Authors

Zhiyi Yuan – School of Electrical and Electronics Engineering, Nanyang Technological University, 639798, Singapore

Xin Cheng – School of Electrical and Electronics Engineering, Nanyang Technological University, 639798, Singapore

Tsungyu Li – School of Electrical and Electronics Engineering, Nanyang Technological University, 639798, Singapore

Yunke Zhou – School of Electrical and Electronics Engineering, Nanyang Technological University, 639798, Singapore

Yifan Zhang – School of Electrical and Electronics Engineering, Nanyang Technological University, 639798, Singapore

Xuerui Gong – School of Electrical and Electronics Engineering, Nanyang Technological University, 639798, Singapore

Guo-En Chang – Department of Mechanical Engineering, and Advanced Institute of Manufacturing with High-Tech Innovations, National Chung Cheng University, Chiayi 62102, Taiwan; orcid.org/0000-0002-3739-5451

Muhammad D. Birowosuto – School of Electrical and Electronics Engineering, Nanyang Technological University, 639798, Singapore; orcid.org/0000-0002-9997-6841

Cuong Dang – School of Electrical and Electronics Engineering, Nanyang Technological University, 639798, Singapore; orcid.org/0000-0001-6183-4082

Complete contact information is available at: <https://pubs.acs.org/10.1021/acsami.1c09845>

Author Contributions

Z.Y. and X.C. contributed equally. Z.Y.: conceptualization, data curation, and writing—original draft preparation. X.C., T.L., Y.Z., Y.Z., and X.G.: investigation, methodology, and software. M.D.B. and C.D.: lifetime measurements. Y.-C.C. and G.-E.C.: funding acquisition, supervision, and writing—review and editing. All the data are available from the corresponding author upon reasonable request.

Notes

The authors declare no competing financial interest.

ACKNOWLEDGMENTS

This research is supported by the Ministry of Education Singapore AcRF Tier-1 2019-T1-002-030 (RG158/19(S)). We would like to thank the lab support from Centre of Bio-Devices and Internal Grant NAP SUG - from NTU.

REFERENCES

- (1) Karl, M.; Meek, A.; Murawski, C.; Tropf, L.; Keum, C.; Schubert, M.; Samuel, I. D. W.; Turnbull, G. A.; Gather, M. C. Distributed Feedback Lasers Based on Green Fluorescent Protein and Conformal High Refractive Index Oxide Layers. *Laser Photon. Rev.* **2020**, *14*, 2000101.
- (2) Dietrich, C. P.; Steude, A.; Tropf, L.; Schubert, M.; Kronenberg, N. M.; Ostermann, K.; Höfling, S.; Gather, M. C. An Exciton-

Polariton Laser Based on Biologically Produced Fluorescent Protein. *Sci. Adv.* **2016**, *2*, No. e1600666.

- (3) Sadeghi, S.; Melikov, R.; Conkar, D.; Firat-Karalar, E. N.; Nizamoglu, S. Ultra-Efficient and High-Quality White Light-Emitting Devices Using Fluorescent Proteins in Aqueous Medium. *Adv. Mater. Technol.* **2020**, *5*, 2000061.

- (4) Zajac, J. M.; Schubert, M.; Roland, T.; Keum, C.; Samuel, I. D. W.; Gather, M. C. Time-Resolved Studies of Energy Transfer in Thin Films of Green and Red Fluorescent Proteins. *Adv. Funct. Mater.* **2018**, *28*, 1706300.

- (5) Dietrich, C. P.; Steude, A.; Schubert, M.; Ohmer, J.; Fischer, U.; Höfling, S.; Gather, M. C. Strong Coupling in Fully Tunable Microcavities Filled with Biologically Produced Fluorescent Proteins. *Adv. Opt. Mater.* **2017**, *5*, 1600659.

- (6) Shimomura, O.; Johnson, F. H.; Saiga, Y. Extraction, Purification and Properties of Aequorin, a Bioluminescent Protein from the Luminous Hydromedusa, *Aequorea*. *J. Cell. Physiol.* **1962**, *59*, 223–239.

- (7) Sidler, W. A. Phycobilisome and Phycobiliprotein Structures. In *The Molecular Biology of Cyanobacteria*; Springer: 1994; pp 139–216.

- (8) Squires, A. H.; Moerner, W. E. Direct Single-Molecule Measurements of Phycocyanobilin Photophysics in Monomeric C-Phycocyanin. *Proc. Natl. Acad. Sci. U.S.A.* **2017**, *114*, 9779–9784.

- (9) Gerster, D.; Reichert, J.; Bi, H.; Barth, J. V.; Kaniber, S. M.; Holleitner, A. W.; Visoly-Fisher, I.; Sergani, S.; Carmeli, I. Photocurrent of a Single Photosynthetic Protein. *Nat. Nanotechnol.* **2012**, *7*, 673–676.

- (10) Das, R.; Kiley, P. J.; Segal, M.; Norville, J.; Yu, A. A.; Wang, L.; Trammell, S. A.; Reddick, L. E.; Kumar, R.; Stellacci, F.; Lebedev, N.; Schnur, J.; Bruce, B. D.; Zhang, S.; Baldo, M. Integration of Photosynthetic Protein Molecular Complexes in Solid-State Electronic Devices. *Nano Lett.* **2004**, *4*, 1079–1083.

- (11) Roxby, D. N.; Rivy, H.; Gong, C.; Gong, X.; Yuan, Z.; Chang, G.-E.; Chen, Y.-C. Microalgae Living Sensor for Metal Ion Detection with Nanocavity-Enhanced Photoelectrochemistry. *Biosens. Bioelectron.* **2020**, *165*, 112420.

- (12) Tan, F.; Wang, N.; Lei, D. Y.; Yu, W.; Zhang, X. Plasmonic Black Absorbers for Enhanced Photocurrent of Visible-Light Photocatalysis. *Adv. Opt. Mater.* **2017**, *5*, 1600399.

- (13) Wang, C.; Zhao, X.-P.; Xu, Q.-Y.; Nie, X.-G.; Younis, M. R.; Liu, W.-Y.; Xia, X.-H. Importance of Hot Spots in Gold Nanostructures on Direct Plasmon-Enhanced Electrochemistry. *ACS Appl. Nano Mater.* **2018**, *1*, 5805–5811.

- (14) Wu, Y.; Yang, W.; Fan, Y.; Song, Q.; Xiao, S. TiO₂ Metasurfaces: From Visible Planar Photonics to Photochemistry. *Sci. Adv.* **2019**, *5*, No. eaax0939.

- (15) Roxby, D. N.; Yuan, Z.; Krishnamoorthy, S.; Wu, P.; Tu, W. C.; Chang, G. E.; Lau, R.; Chen, Y. C. Enhanced Biophotocurrent Generation in Living Photosynthetic Optical Resonator. *Adv. Sci.* **2020**, *7*, 1903707.

- (16) Grandidier, J.; Callahan, D. M.; Munday, J. N.; Atwater, H. A. Light Absorption Enhancement in Thin-Film Solar Cells Using Whispering Gallery Modes in Dielectric Nanospheres. *Adv. Mater.* **2011**, *23*, 1272–1276.

- (17) Sergeant, N. P.; Hadipour, A.; Niesen, B.; Cheyns, D.; Heremans, P.; Peumans, P.; Rand, B. P. Design of Transparent Anodes for Resonant Cavity Enhanced Light Harvesting in Organic Solar Cells. *Adv. Mater.* **2012**, *24*, 728–732.

- (18) Shi, X.; Ueno, K.; Oshikiri, T.; Sun, Q.; Sasaki, K.; Misawa, H. Enhanced Water Splitting under Modal Strong Coupling Conditions. *Nat. Nanotechnol.* **2018**, *13*, 953–958.

- (19) Vollmer, F.; Arnold, S. Whispering-Gallery-Mode Biosensing: Label-Free Detection Down to Single Molecules. *Nat. Methods* **2008**, *5*, 591–596.

- (20) He, L.; Özdemir, Ş. K.; Zhu, J.; Kim, W.; Yang, L. Detecting Single Viruses and Nanoparticles Using Whispering Gallery Micro-lasers. *Nat. Nanotechnol.* **2011**, *6*, 428–432.

- (21) Zhu, J.; Ozdemir, S. K.; Xiao, Y.-F.; Li, L.; He, L.; Chen, D.-R.; Yang, L. On-Chip Single Nanoparticle Detection and Sizing by Mode

- Splitting in an Ultrahigh-Q Microresonator. *Nat. Photonics* **2010**, *4*, 46–49.
- (22) Schubert, M.; Woolfson, L.; Barnard, I. R.; Dorward, A. M.; Casement, B.; Morton, A.; Robertson, G. B.; Appleton, P. L.; Miles, G. B.; Tucker, C. S.; Gather, M. C. Monitoring Contractility in Cardiac Tissue with Cellular Resolution Using Biointegrated Microlasers. *Nat. Photonics* **2020**, *14*, 452.
- (23) Schubert, M.; Steude, A.; Liehm, P.; Kronenberg, N. M.; Karl, M.; Campbell, E. C.; Powis, S. J.; Gather, M. C. Lasing within Live Cells Containing Intracellular Optical Micro-Resonators for Barcode-Type Cell Tagging and Tracking. *Nano Lett.* **2015**, *15*, 5647–5652.
- (24) Schaafsma, B. E.; Mieog, J. S. D.; Hutteman, M.; Van der Vorst, J. R.; Kuppen, P. J. K.; Löwik, C. W. G. M.; Frangioni, J. V.; Van de Velde, C. J. H.; Vahrmeijer, A. L. The Clinical Use of Indocyanine Green as a near-Infrared Fluorescent Contrast Agent for Image-Guided Oncologic Surgery. *J. Surg. Oncol.* **2011**, *104*, 323–332.
- (25) Pan, T.; Lu, D.; Xin, H.; Li, B. Biophotonic Probes for Bio-Detection and Imaging. *Light Sci. Appl.* **2021**, *10*, 124.
- (26) Das, T. K.; Ilaiyaraja, P.; Sudakar, C. Whispering Gallery Mode Assisted Enhancement in the Power Conversion Efficiency of Dssc and Qdssc Devices Using Tio2 Microsphere Photoanodes. *ACS Appl. Energy Mater.* **2018**, *1*, 765–774.
- (27) Dakshinamurthy, A. C.; Das, T. K.; Ilaiyaraja, P.; Sudakar, C. Quantum Dot Sensitized Whisperonic Solar Cells-Improving Efficiency through Whispering Gallery Modes. *Front. Mater.* **2019**, *6*, 282.
- (28) Wang, Y.; Li, M.; Zhou, X.; Li, P.; Hu, X.; Song, Y. High Efficient Perovskite Whispering-Gallery Solar Cells. *Nano Energy* **2018**, *51*, 556–562.
- (29) Zhang, J.; Jin, X.; Morales-Guzman, P. I.; Yu, X.; Liu, H.; Zhang, H.; Razzari, L.; Claverie, J. P. Engineering the Absorption and Field Enhancement Properties of Au–Tio2 Nanohybrids Via Whispering Gallery Mode Resonances for Photocatalytic Water Splitting. *ACS Nano* **2016**, *10*, 4496–4503.
- (30) Fan, X.; Yun, S.-H. The Potential of Optofluidic Biolasers. *Nat. Methods* **2014**, *11*, 141–147.
- (31) Chen, Y.-C.; Tan, X.; Sun, Q.; Chen, Q.; Wang, W.; Fan, X. Laser-Emission Imaging of Nuclear Biomarkers for High-Contrast Cancer Screening and Immunodiagnosis. *Nat. Biomed. Eng.* **2017**, *1*, 724–735.
- (32) Humar, M.; Hyun Yun, S. Intracellular Microlasers. *Nat. Photonics* **2015**, *9*, 572–576.
- (33) Chen, Y. C.; Fan, X. Biological Lasers for Biomedical Applications. *Adv. Opt. Mater.* **2019**, *7*, 1900377.
- (34) Ta, V. D.; Caixeiro, S.; Fernandes, F. M.; Sapienza, R. Microsphere Solid-State Biolasers. *Adv. Opt. Mater.* **2017**, *5*, 1601022.
- (35) Yuan, Z.; Wang, Z.; Guan, P.; Wu, X.; Chen, Y. C. Lasing-Encoded Microsensor Driven by Interfacial Cavity Resonance Energy Transfer. *Adv. Opt. Mater.* **2020**, *8*, 1901596.
- (36) Rivera, J. A.; Eden, J. G. Lasing at 602–620 Nm from a Red Algae-Derived Phycobiliprotein. *APL Photonics* **2017**, *2*, 121301.
- (37) Yoshino, K.; Yamashiro, K.; Inuishi, Y. Electrical Conductivity in Cholesteric Liquid Crystals. *Jpn. J. Appl. Phys.* **1974**, *13*, 1471.
- (38) Schiro, P. G.; Kwok, A. S. Cavity-Enhanced Emission from a Dye-Coated Microsphere. *Opt. Express* **2004**, *12*, 2857–2863.
- (39) Humar, M.; Yun, S. H. Whispering-Gallery-Mode Emission from Biological Luminescent Protein Microcavity Assemblies. *Optica* **2017**, *4*, 222–228.
- (40) Riesen, N.; Reynolds, T.; François, A.; Henderson, M. R.; Monro, T. M. Q-Factor Limits for Far-Field Detection of Whispering Gallery Modes in Active Microspheres. *Opt. express* **2015**, *23*, 28896–28904.
- (41) Annadhasan, M.; Venkataramudu, U.; Mitetelo, N. V.; Mamonov, E. A.; Sahoo, C.; Naraharisetty, S. R. G.; Murzina, T. V.; Chandrasekar, R. High Optical Energy Storage and Two-Photon Luminescence from Solution-Processed Perovskite-Polystyrene Composite Microresonators. *ACS Appl. Energy Mater.* **2018**, *2*, 428–435.
- (42) Zhang, Y.; Zhang, C.; Fan, Y.; Liu, Z.; Hu, F.; Zhao, Y. S. Smart Protein-Based Biolasers: An Alternative Way to Protein Conformation Detection. *ACS Appl. Mater. Interfaces* **2021**, *13*, 19187–19192.
- (43) Jeong, Y.; Schatz, G. C. Enhancement and Suppression of Resonance Energy Transfer near Metal Nanoparticles. *J. Phys. Chem. C* **2020**, *124*, 20589–20597.
- (44) Hsu, L.-Y.; Ding, W.; Schatz, G. C. Plasmon-Coupled Resonance Energy Transfer. *J. Phys. Chem. Lett.* **2017**, *8*, 2357–2367.
- (45) Ding, W.; Hsu, L.-Y.; Heaps, C. W.; Schatz, G. C. Plasmon-Coupled Resonance Energy Transfer II: Exploring the Peaks and Dips in the Electromagnetic Coupling Factor. *J. Phys. Chem. C* **2018**, *122*, 22650–22659.
- (46) Yuan, Z.; Tan, X.; Gong, X.; Gong, C.; Cheng, X.; Feng, S.; Fan, X.; Chen, Y.-C. Bioresponsive Microlasers with Tunable Lasing Wavelength. *Nanoscale* **2021**, *13*, 1608–1615.
- (47) Zhou, Y.; Yuan, Z.; Gong, X.; Birowosuto, M. D.; Dang, C. H.; Chen, Y.-C. Dynamic Photonic Barcodes for Molecular Detection Based on Cavity-Enhanced Energy Transfer. *Adv. Photonics* **2020**, *2*, 066002.
- (48) Jana, S.; Xu, X.; Klymchenko, A.; Reisch, A.; Pons, T. Microcavity-Enhanced Fluorescence Energy Transfer from Quantum Dot Excited Whispering Gallery Modes to Acceptor Dye Nanoparticles. *ACS Nano* **2020**, *15*, 1445–1453.
- (49) Kfir, O.; Lourenço-Martins, H.; Storeck, G.; Sivi, M.; Harvey, T. R.; Kippenberg, T. J.; Feist, A.; Ropers, C. Controlling Free Electrons with Optical Whispering-Gallery Modes. *Nature* **2020**, *582*, 46–49.
- (50) Zhao, Y.; Wyrick, J.; Natterer, F. D.; Rodriguez-Nieva, J. F.; Lewandowski, C.; Watanabe, K.; Taniguchi, T.; Levitov, L. S.; Zhitenev, N. B.; Stroschio, J. A. Creating and Probing Electron Whispering-Gallery Modes in Graphene. *Science* **2015**, *348*, 672–675.
- (51) Coles, D.; Flatten, L. C.; Sydney, T.; Hounslow, E.; Saikin, S. K.; Aspuru-Guzik, A.; Vedral, V.; Tang, J. K. H.; Taylor, R. A.; Smith, J. M.; Lidzey, D. G. A Nanophotonic Structure Containing Living Photosynthetic Bacteria. *Small* **2017**, *13*, 1701777.
- (52) Coles, D. M.; Yang, Y.; Wang, Y.; Grant, R. T.; Taylor, R. A.; Saikin, S. K.; Aspuru-Guzik, A.; Lidzey, D. G.; Tang, J. K.-H.; Smith, J. M. Strong Coupling between Chlorosomes of Photosynthetic Bacteria and a Confined Optical Cavity Mode. *Nat. Commun.* **2014**, *5*, 5561.
- (53) Miller, T. E.; Beneyton, T.; Schwander, T.; Diehl, C.; Girault, M.; McLean, R.; Chotel, T.; Claus, P.; Cortina, N. S.; Baret, J.-C.; Erb, T. J. Light-Powered Co2 Fixation in a Chloroplast Mimic with Natural and Synthetic Parts. *Science* **2020**, *368*, 649–654.
- (54) Hall, J. M. M.; Shahaam Afshar, V.; Henderson, M. R.; François, A.; Reynolds, T.; Riesen, N.; Monro, T. M. Method for Predicting Whispering Gallery Mode Spectra of Spherical Microresonators. *Opt. Express* **2015**, *23*, 9924–9937.